

This article was downloaded by:

On: 31 January 2011

Access details: *Access Details: Free Access*

Publisher *Taylor & Francis*

Informa Ltd Registered in England and Wales Registered Number: 1072954 Registered office: Mortimer House, 37-41 Mortimer Street, London W1T 3JH, UK

MOLECULAR CRYSTALS AND LIQUID CRYSTALS	
Volume 442 • 2010	
CONTENTS	
Liquid Crystals	
Structural Analysis of Hexamethyl Pairs in Nematic Liquid Crystals	1
V. A. Podkoren, V. A. Malozemov, I. A. Gilevskiy, A. P. Mikhlin, I. A. Rudakovskiy, V. P. Kabanov, A. A. Zolotarev, and M. I. Shchegolev	
Temperature-Dependent Penetration of Polymers into Crystalline Liquid Crystals Embedded in Cellulose Matrix Structures	10
Ramona Dancu, Elena Kholodovskaya, and Patrick Attali	
Optical Structure of an Anisotropic Viscoelastic Polymer in Nematic Liquid Crystals	21
A. S. Kabanov, M. N. Ponomareva, and M. A. Kabanov	
Liquid Crystal Alignment on Anisotropic Nanoporous Films	41
Y. H. Kim and C. A. Ochoa	
Surface Coating of Nematic Liquid Crystals on Polymer Substrates	51
Y. H. Kim and C. A. Ochoa	
Surface Coating of Nematic Liquid Crystals on Polymer Substrates	61
Y. H. Kim and C. A. Ochoa	
Surface Coating of Nematic Liquid Crystals on Polymer Substrates	71
Y. H. Kim and C. A. Ochoa	
Surface Coating of Nematic Liquid Crystals on Polymer Substrates	81
Y. H. Kim and C. A. Ochoa	
Surface Coating of Nematic Liquid Crystals on Polymer Substrates	91
Y. H. Kim and C. A. Ochoa	
Surface Coating of Nematic Liquid Crystals on Polymer Substrates	101
Y. H. Kim and C. A. Ochoa	
Surface Coating of Nematic Liquid Crystals on Polymer Substrates	111
Y. H. Kim and C. A. Ochoa	
Surface Coating of Nematic Liquid Crystals on Polymer Substrates	121
Y. H. Kim and C. A. Ochoa	
Surface Coating of Nematic Liquid Crystals on Polymer Substrates	131
Y. H. Kim and C. A. Ochoa	
Surface Coating of Nematic Liquid Crystals on Polymer Substrates	141
Y. H. Kim and C. A. Ochoa	
Surface Coating of Nematic Liquid Crystals on Polymer Substrates	151
Y. H. Kim and C. A. Ochoa	
Surface Coating of Nematic Liquid Crystals on Polymer Substrates	161
Y. H. Kim and C. A. Ochoa	
Surface Coating of Nematic Liquid Crystals on Polymer Substrates	171
Y. H. Kim and C. A. Ochoa	
Surface Coating of Nematic Liquid Crystals on Polymer Substrates	181
Y. H. Kim and C. A. Ochoa	
Surface Coating of Nematic Liquid Crystals on Polymer Substrates	191
Y. H. Kim and C. A. Ochoa	
Surface Coating of Nematic Liquid Crystals on Polymer Substrates	201
Y. H. Kim and C. A. Ochoa	
Surface Coating of Nematic Liquid Crystals on Polymer Substrates	211
Y. H. Kim and C. A. Ochoa	
Surface Coating of Nematic Liquid Crystals on Polymer Substrates	221
Y. H. Kim and C. A. Ochoa	
Surface Coating of Nematic Liquid Crystals on Polymer Substrates	231
Y. H. Kim and C. A. Ochoa	
Surface Coating of Nematic Liquid Crystals on Polymer Substrates	241
Y. H. Kim and C. A. Ochoa	
Surface Coating of Nematic Liquid Crystals on Polymer Substrates	251
Y. H. Kim and C. A. Ochoa	
Surface Coating of Nematic Liquid Crystals on Polymer Substrates	261
Y. H. Kim and C. A. Ochoa	
Surface Coating of Nematic Liquid Crystals on Polymer Substrates	271
Y. H. Kim and C. A. Ochoa	
Surface Coating of Nematic Liquid Crystals on Polymer Substrates	281
Y. H. Kim and C. A. Ochoa	
Surface Coating of Nematic Liquid Crystals on Polymer Substrates	291
Y. H. Kim and C. A. Ochoa	
Surface Coating of Nematic Liquid Crystals on Polymer Substrates	301
Y. H. Kim and C. A. Ochoa	
Surface Coating of Nematic Liquid Crystals on Polymer Substrates	311
Y. H. Kim and C. A. Ochoa	
Surface Coating of Nematic Liquid Crystals on Polymer Substrates	321
Y. H. Kim and C. A. Ochoa	
Surface Coating of Nematic Liquid Crystals on Polymer Substrates	331
Y. H. Kim and C. A. Ochoa	
Surface Coating of Nematic Liquid Crystals on Polymer Substrates	341
Y. H. Kim and C. A. Ochoa	
Surface Coating of Nematic Liquid Crystals on Polymer Substrates	351
Y. H. Kim and C. A. Ochoa	
Surface Coating of Nematic Liquid Crystals on Polymer Substrates	361
Y. H. Kim and C. A. Ochoa	
Surface Coating of Nematic Liquid Crystals on Polymer Substrates	371
Y. H. Kim and C. A. Ochoa	
Surface Coating of Nematic Liquid Crystals on Polymer Substrates	381
Y. H. Kim and C. A. Ochoa	
Surface Coating of Nematic Liquid Crystals on Polymer Substrates	391
Y. H. Kim and C. A. Ochoa	
Surface Coating of Nematic Liquid Crystals on Polymer Substrates	401
Y. H. Kim and C. A. Ochoa	
Surface Coating of Nematic Liquid Crystals on Polymer Substrates	411
Y. H. Kim and C. A. Ochoa	
Surface Coating of Nematic Liquid Crystals on Polymer Substrates	421
Y. H. Kim and C. A. Ochoa	
Surface Coating of Nematic Liquid Crystals on Polymer Substrates	431
Y. H. Kim and C. A. Ochoa	
Surface Coating of Nematic Liquid Crystals on Polymer Substrates	441
Y. H. Kim and C. A. Ochoa	
Surface Coating of Nematic Liquid Crystals on Polymer Substrates	451
Y. H. Kim and C. A. Ochoa	
Surface Coating of Nematic Liquid Crystals on Polymer Substrates	461
Y. H. Kim and C. A. Ochoa	
Surface Coating of Nematic Liquid Crystals on Polymer Substrates	471
Y. H. Kim and C. A. Ochoa	
Surface Coating of Nematic Liquid Crystals on Polymer Substrates	481
Y. H. Kim and C. A. Ochoa	
Surface Coating of Nematic Liquid Crystals on Polymer Substrates	491
Y. H. Kim and C. A. Ochoa	
Surface Coating of Nematic Liquid Crystals on Polymer Substrates	501
Y. H. Kim and C. A. Ochoa	
Surface Coating of Nematic Liquid Crystals on Polymer Substrates	511
Y. H. Kim and C. A. Ochoa	
Surface Coating of Nematic Liquid Crystals on Polymer Substrates	521
Y. H. Kim and C. A. Ochoa	
Surface Coating of Nematic Liquid Crystals on Polymer Substrates	531
Y. H. Kim and C. A. Ochoa	
Surface Coating of Nematic Liquid Crystals on Polymer Substrates	541
Y. H. Kim and C. A. Ochoa	
Surface Coating of Nematic Liquid Crystals on Polymer Substrates	551
Y. H. Kim and C. A. Ochoa	
Surface Coating of Nematic Liquid Crystals on Polymer Substrates	561
Y. H. Kim and C. A. Ochoa	
Surface Coating of Nematic Liquid Crystals on Polymer Substrates	571
Y. H. Kim and C. A. Ochoa	
Surface Coating of Nematic Liquid Crystals on Polymer Substrates	581
Y. H. Kim and C. A. Ochoa	
Surface Coating of Nematic Liquid Crystals on Polymer Substrates	591
Y. H. Kim and C. A. Ochoa	
Surface Coating of Nematic Liquid Crystals on Polymer Substrates	601
Y. H. Kim and C. A. Ochoa	
Surface Coating of Nematic Liquid Crystals on Polymer Substrates	611
Y. H. Kim and C. A. Ochoa	
Surface Coating of Nematic Liquid Crystals on Polymer Substrates	621
Y. H. Kim and C. A. Ochoa	
Surface Coating of Nematic Liquid Crystals on Polymer Substrates	631
Y. H. Kim and C. A. Ochoa	
Surface Coating of Nematic Liquid Crystals on Polymer Substrates	641
Y. H. Kim and C. A. Ochoa	
Surface Coating of Nematic Liquid Crystals on Polymer Substrates	651
Y. H. Kim and C. A. Ochoa	
Surface Coating of Nematic Liquid Crystals on Polymer Substrates	661
Y. H. Kim and C. A. Ochoa	
Surface Coating of Nematic Liquid Crystals on Polymer Substrates	671
Y. H. Kim and C. A. Ochoa	
Surface Coating of Nematic Liquid Crystals on Polymer Substrates	681
Y. H. Kim and C. A. Ochoa	
Surface Coating of Nematic Liquid Crystals on Polymer Substrates	691
Y. H. Kim and C. A. Ochoa	
Surface Coating of Nematic Liquid Crystals on Polymer Substrates	701
Y. H. Kim and C. A. Ochoa	
Surface Coating of Nematic Liquid Crystals on Polymer Substrates	711
Y. H. Kim and C. A. Ochoa	
Surface Coating of Nematic Liquid Crystals on Polymer Substrates	721
Y. H. Kim and C. A. Ochoa	
Surface Coating of Nematic Liquid Crystals on Polymer Substrates	731
Y. H. Kim and C. A. Ochoa	
Surface Coating of Nematic Liquid Crystals on Polymer Substrates	741
Y. H. Kim and C. A. Ochoa	
Surface Coating of Nematic Liquid Crystals on Polymer Substrates	751
Y. H. Kim and C. A. Ochoa	
Surface Coating of Nematic Liquid Crystals on Polymer Substrates	761
Y. H. Kim and C. A. Ochoa	
Surface Coating of Nematic Liquid Crystals on Polymer Substrates	771
Y. H. Kim and C. A. Ochoa	
Surface Coating of Nematic Liquid Crystals on Polymer Substrates	781
Y. H. Kim and C. A. Ochoa	
Surface Coating of Nematic Liquid Crystals on Polymer Substrates	791
Y. H. Kim and C. A. Ochoa	
Surface Coating of Nematic Liquid Crystals on Polymer Substrates	801
Y. H. Kim and C. A. Ochoa	
Surface Coating of Nematic Liquid Crystals on Polymer Substrates	811
Y. H. Kim and C. A. Ochoa	
Surface Coating of Nematic Liquid Crystals on Polymer Substrates	821
Y. H. Kim and C. A. Ochoa	
Surface Coating of Nematic Liquid Crystals on Polymer Substrates	831
Y. H. Kim and C. A. Ochoa	
Surface Coating of Nematic Liquid Crystals on Polymer Substrates	841
Y. H. Kim and C. A. Ochoa	
Surface Coating of Nematic Liquid Crystals on Polymer Substrates	851
Y. H. Kim and C. A. Ochoa	
Surface Coating of Nematic Liquid Crystals on Polymer Substrates	861
Y. H. Kim and C. A. Ochoa	
Surface Coating of Nematic Liquid Crystals on Polymer Substrates	871
Y. H. Kim and C. A. Ochoa	
Surface Coating of Nematic Liquid Crystals on Polymer Substrates	881
Y. H. Kim and C. A. Ochoa	
Surface Coating of Nematic Liquid Crystals on Polymer Substrates	891
Y. H. Kim and C. A. Ochoa	
Surface Coating of Nematic Liquid Crystals on Polymer Substrates	901
Y. H. Kim and C. A. Ochoa	
Surface Coating of Nematic Liquid Crystals on Polymer Substrates	911
Y. H. Kim and C. A. Ochoa	
Surface Coating of Nematic Liquid Crystals on Polymer Substrates	921
Y. H. Kim and C. A. Ochoa	
Surface Coating of Nematic Liquid Crystals on Polymer Substrates	931
Y. H. Kim and C. A. Ochoa	
Surface Coating of Nematic Liquid Crystals on Polymer Substrates	941
Y. H. Kim and C. A. Ochoa	
Surface Coating of Nematic Liquid Crystals on Polymer Substrates	951
Y. H. Kim and C. A. Ochoa	
Surface Coating of Nematic Liquid Crystals on Polymer Substrates	961
Y. H. Kim and C. A. Ochoa	
Surface Coating of Nematic Liquid Crystals on Polymer Substrates	971
Y. H. Kim and C. A. Ochoa	
Surface Coating of Nematic Liquid Crystals on Polymer Substrates	981
Y. H. Kim and C. A. Ochoa	
Surface Coating of Nematic Liquid Crystals on Polymer Substrates	991
Y. H. Kim and C. A. Ochoa	
Surface Coating of Nematic Liquid Crystals on Polymer Substrates	1001
Y. H. Kim and C. A. Ochoa	

## Molecular Crystals and Liquid Crystals

Publication details, including instructions for authors and subscription information:

<http://www.informaworld.com/smpp/title~content=t713644168>

### Dynamic Fringe Pattern Generation Using an Electrically Tunable Liquid Crystal Fabry-Perot Cell for a Miniaturized Optical 3-D Surface Scanning Profilometer

Chang-Sub Park<sup>a</sup>; Kyung-Woo Park<sup>b</sup>; Unsang Jung<sup>b</sup>; Jeehyun Kim<sup>b</sup>; Shin-Won Kang<sup>ab</sup>; Hak-Rin Kim<sup>ab</sup>

<sup>a</sup> Department of Sensor and Display Engineering, Kyungpook National University, Daegu, Korea <sup>b</sup>

School of Electrical Engineering and Computer Science, Kyungpook National University, Daegu, Korea

First published on: 19 August 2010

**To cite this Article** Park, Chang-Sub , Park, Kyung-Woo , Jung, Unsang , Kim, Jeehyun , Kang, Shin-Won and Kim, Hak-Rin(2010) 'Dynamic Fringe Pattern Generation Using an Electrically Tunable Liquid Crystal Fabry-Perot Cell for a Miniaturized Optical 3-D Surface Scanning Profilometer', *Molecular Crystals and Liquid Crystals*, 526: 1, 28 — 37

**To link to this Article:** DOI: 10.1080/15421406.2010.485065

**URL:** <http://dx.doi.org/10.1080/15421406.2010.485065>

PLEASE SCROLL DOWN FOR ARTICLE

Full terms and conditions of use: <http://www.informaworld.com/terms-and-conditions-of-access.pdf>

This article may be used for research, teaching and private study purposes. Any substantial or systematic reproduction, re-distribution, re-selling, loan or sub-licensing, systematic supply or distribution in any form to anyone is expressly forbidden.

The publisher does not give any warranty express or implied or make any representation that the contents will be complete or accurate or up to date. The accuracy of any instructions, formulae and drug doses should be independently verified with primary sources. The publisher shall not be liable for any loss, actions, claims, proceedings, demand or costs or damages whatsoever or howsoever caused arising directly or indirectly in connection with or arising out of the use of this material.

# Dynamic Fringe Pattern Generation Using an Electrically Tunable Liquid Crystal Fabry-Perot Cell for a Miniaturized Optical 3-D Surface Scanning Profilometer

CHANG-SUB PARK,<sup>1</sup> KYUNG-WOO PARK,<sup>2</sup>  
UNSANG JUNG,<sup>2</sup> JEEHYUN KIM,<sup>2</sup>  
SHIN-WON KANG,<sup>1,2</sup> AND HAK-RIN KIM<sup>1,2</sup>

<sup>1</sup>Department of Sensor and Display Engineering, Kyungpook National University, Daegu, Korea

<sup>2</sup>School of Electrical Engineering and Computer Science, Kyungpook National University, Daegu, Korea

*We demonstrated a dynamic fringe pattern generation method by using an electrically tunable liquid crystal (LC) Fabry-Perot (FP) cell. In our LC-FP cell, the multiple interferences within the cavity produce concentric ring-type patterns projected on a flat surface because the resonant mode conditions determined by the optical path lengths are circularly symmetric to the slightly diverging single input beam. The projected fringe patterns can be continuously varied with increasing the diameters of the interference rings since the resonant mode conditions can be electrically controlled by changing the effective refractive index of the LC layer. The resonant mode analysis shows that the real surface profiles can be obtained by comparing the amount of distortions of the projected fringe patterns. Our dynamic fringe pattern generation properties, achieved by using single input beam and single LC-FP cell, can be used for miniaturizing optical 3-D surface scanning profilometers.*

**Keywords** Fabry-Perot; interference pattern; liquid crystal; optical surface profilometer; resonant mode

## Introduction

A 3D surface profilometer is a device for extracting an accurate depth profile from an object surface, which is used for an industrial inspection and a medical diagnosis. The surface profile can be obtained by using the direct contact measurement methods such as an atomic force microscopy and a scanning tunneling microscopy.

The contact measurement methods show high precision in depth profile but their measurement speeds are too slow which should scan a surface with a moving tip in a

---

Address correspondence to Hak-Rin Kim, School of Electrical Engineering and Computer Science, Kyungpook National University, Daegu 702-701, Korea. E-mail: rineey@ee.knu.ac.kr

point. In addition, the contact methods are not suitable for the bio-medical imaging to living organs or tissues, which can induce damages on the object during measurement.

As for the non-contact method for measuring surface profiles, there are optical 3D surface profilometers which measure 3D shapes of a reflective object by analyzing distortions of the projected fringe patterns. The optical methods can measure the surface profile of a soft material surface in a nondestructive manner with a relatively faster measuring speed by analyzing depth profiles from a whole optical pattern. In constructing optical surface profilometers, an optical instrument for generating and projecting fringe patterns on an object is a key optical component. Analyzing schemes are different depending on generation methods of the fringe patterns and origins of the fringe distortions. In interferometric methods [1], sinusoidal fringe pattern from two-beam coupling is used. In this case, there exists phase ambiguity in analyzing the surface map when depth difference of an object surface in physical length is higher than phase difference of  $2\pi$ . To reduce the phase ambiguity of the surface map from the distortions of the projected fringes, several sets of fringe patterns are required which can be generated by phase-shifting techniques [2,3] using spatial light modulators. In digital fringe projection methods [4], surface map is reconstructed by analyzing multiple sets of fringe patterns distorted by a surface profile. Therefore, digital projector or a liquid crystal display (LCD) panel [4,5] is also required to get sufficient information from the distorted patterns. However, the conventional fringe pattern generators for optical 3D surface profilometers were too bulky and too expensive to implement a miniaturized 3D surface profilometer for hand-held type medical applications [5].

In this paper, we show that multiple sets of concentric ring-type fringe patterns can be obtained by using single LC Fabry-Perot (FP) cell, where the fringe patterns were generated by multiple interferences from a slightly diverging single input beam. Recently, there have been so many reports on electrically wavelength-tunable LC-FP cells [6–12]. However, the functions and their analysis were only focused on the wavelength tuning properties using normally incident broadband light source, where the applications were limited on tunable filters especially for optical communications. In those cases, the resonant mode analysis and their polarization dependence were fully described. Whereas, there have been no report on the analysis of the resonant mode and the dynamic fringe patterns when the diverging beam is incident on an electrically tunable LC-FP cell. In this paper, we demonstrated the resonant mode analysis in an LC-FP cell depending on the ray directions relative to the optic axis of the active LC layer by modifying the fringe pattern analysis in a conventional FP cell [13]. In our LC-FP cell, the projected fringe patterns can be continuously varied with increasing the diameters of the interference rings since the resonant mode conditions can be electrically controlled by changing the effective refractive index of the LC layer between the cavity mirrors. The resonant mode analysis shows that the real surface profile can be obtained by comparing the amount of distortions of the fringe patterns with the designed fringe patterns from the analytical model. The surface profilometer can be simply miniaturized because the dynamic fringe patterns are constructed only by single beam and single cell structure in our approach. Especially, it is expected that our optical surface profilometer system can be widely applied in environmental and bio-medical areas because it can do fast measurement by using electro-optic effect of LC without any damage on a measuring surface.

## Device Schemes

Figures 1(a) and (b) show the structure of the fabricated LC-FP device and the generated fringe patterns on a flat surface at a normal incident condition by using the proposed LC-FP cell, respectively. The one substrate of the LC-FP cell had stacked layers with ITO glass, dielectric mirror layer, and homeotropic LC alignment layer. The other substrate was stacked with homeotropic LC layer, ITO glass, and dielectric mirror layer. The LC alignment layers were mechanically rubbed with anti-parallel directions. Between the LC alignment layers, a nematic LC (NLC) with a negative dielectric anisotropy was filled to the NLC-FP cell, where the refractive indexes were  $n_o = 1.4747$  and  $n_e = 1.5571$ .

Thus, the NLC-FP cavity was formed by the electrically tunable NLC layer ( $d_{lc}$ ) and the thick glass layer ( $d_g$ ) between the dielectric mirrors. The total thickness of the FP cavity gives as follows:  $d = d_{lc} + d_g$ . When the gap within the cavity is too small, the resolution of surface profilometer is very poor due to the wide distance between fringe patterns. However, we cannot increase the cavity gap sufficiently with only the NLC layer considering the stability of the LC alignment and the response time of the NLC layer. Therefore, the cavity gap was increased by the glass layer in our structure. We fabricated the two types of the NLC-FP cells with different LC layer thickness of  $6\ \mu\text{m}$  and  $15\ \mu\text{m}$ . In both samples, the thickness of the glass layer within the FP cavity was  $700\ \mu\text{m}$ . The reflectance of the dielectric mirrors were 50% and

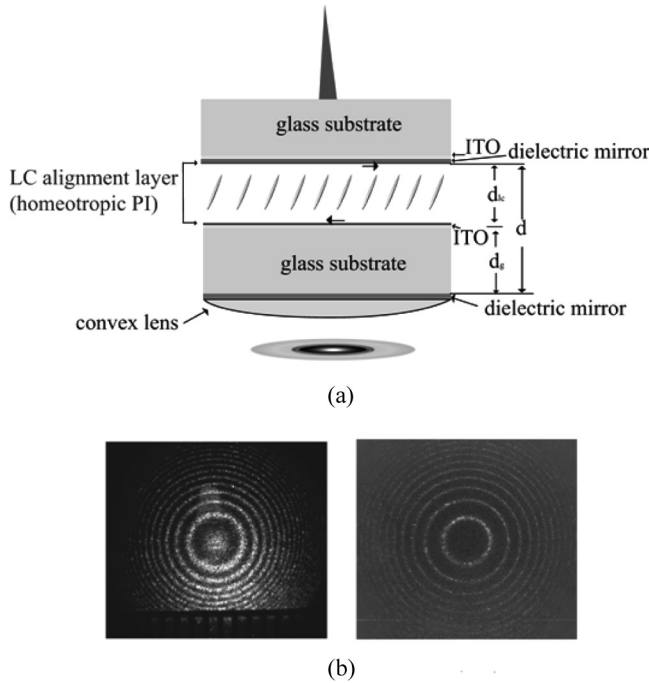


**Figure 1.** (a) The schematic diagram of the proposed NLC-FP cell, and (b) the projected fringe patterns on a flat surface at a normal incident condition, which is observed without an applied voltage to the LC-FP cell. The left and right images are the projected fringe patterns obtained with the cell conditions of the lower mirror reflectance (50%) and the lower LC cell gap ( $d_{lc} = 6\ \mu\text{m}$ ), and the higher mirror reflectance (95%) and the higher LC cell gap ( $d_{lc} = 15\ \mu\text{m}$ ), respectively.

95% in two samples of the LC layer thickness of 6  $\mu\text{m}$  and 15  $\mu\text{m}$ , respectively. The line width of fringe patterns should be sharp to obtain precise 3D surface map in measuring surface profiles with optical scanning methods. As shown in Figure 1(b), a higher reflectance mirror is suitable in our system.

When we irradiate a polarized diverging beam to the NLC-FP cell without an applied voltage, the LC-FP cell with vertically aligned NLC geometry produces nonperiodic concentric circular interference patterns because the resonant mode conditions determined by the optical path lengths are circularly symmetric to the slightly diverging single input beam as shown in Figure 1(b). When we apply voltages to the NLC-FP cell, optical paths of extraordinary rays are changed due to dielectric anisotropy of the NLC, whereas optical paths of ordinary rays are not changed. Thus, the incident beam should be linearly polarized parallel to the rubbing direction of the LC alignment layer to control the resonant conditions. The phase delay,  $\delta$  of the LC-FP cavity is expressed as follows in our NLC-FP cell [13,14].

$$\delta = 4\pi d_{lc} n_{eff} \cos \phi_{lc} + 4\pi d_g n_g \cos \phi_g \quad (1)$$

$$\left(\frac{1}{n_{eff}}\right)^2 = \frac{\cos^2(\theta_{lc} - \phi_{lc})}{n_0^2} + \frac{\sin^2(\theta_{lc} - \phi_{lc})}{n_e^2} \quad (2)$$

where  $n_{eff}$  and  $n_g$  are the effective refractive index of the LC layer and the refractive index of the ITO glass layer, respectively.  $\phi_{lc}$  is the incident angle to the normal direction on the reflective mirror surface adjacent to the LC layer.  $\phi_g$  is the incident angle to the normal direction on the reflective mirror surface adjacent to the glass layer in the bottom substrate as shown in Figure 1(a).  $\theta_{lc}$  is the tilting angle of the LC director to the substrate. Here,  $\theta_{lc}$  and  $n_{eff}$  are the voltage-dependent parameters.

Figure 2 shows the dynamic fringe patterns observed by varying applied voltages where the image plane was flat and parallel to the LC-FP cell as shown in Figure 1(a). Figure 2(a) was obtained at the NLC-FP cell which was made by the lower reflectance mirror (50% reflectance) and lower LC cell gap of ( $d_{lc} = 6 \mu\text{m}$ ). Figure 2(b) was the projected image of the cell using 95% reflectance mirror and the 15  $\mu\text{m}$  LC cell gap. In the field-on state, the LC is tilted along the rubbing direction.

Therefore, there is small difference in both  $\phi_{lc}$  and  $\phi_g$  depending on the propagation direction of the incident light. However, the diverging angle of the incident beam is so small ( $<0.2^\circ$ ) that the projected fringe patterns show circularly ring patterns in the whole driving voltages. Actually, the fringe patterns shown in Figure 2 were obtained by the rays within the diverging angle of  $0.001^\circ$  among the incident diverging beam in our experimental condition, which was obtained by the ray tracing method. The multiple reflections of the rays within the cavity are another reason for the circularly symmetric fringe pattern in our NLC-FP system.

Due to variation of the effective refractive index of the LC layer, the projected fringe patterns are dynamically moving outward from the center of the projection by increasing applied voltages to the NLC-FP cell. In our vertically aligned LC geometry, the radius,  $R_p$ , of the fringe ring at each resonant order is increased due to the increased optical path within the cavity. Here,  $p$  denotes the order of the bright fringe rings from the center of the projected patterns [13]. When we compare the projected images from two NLC-FP cells, the variations of the ring diameters in

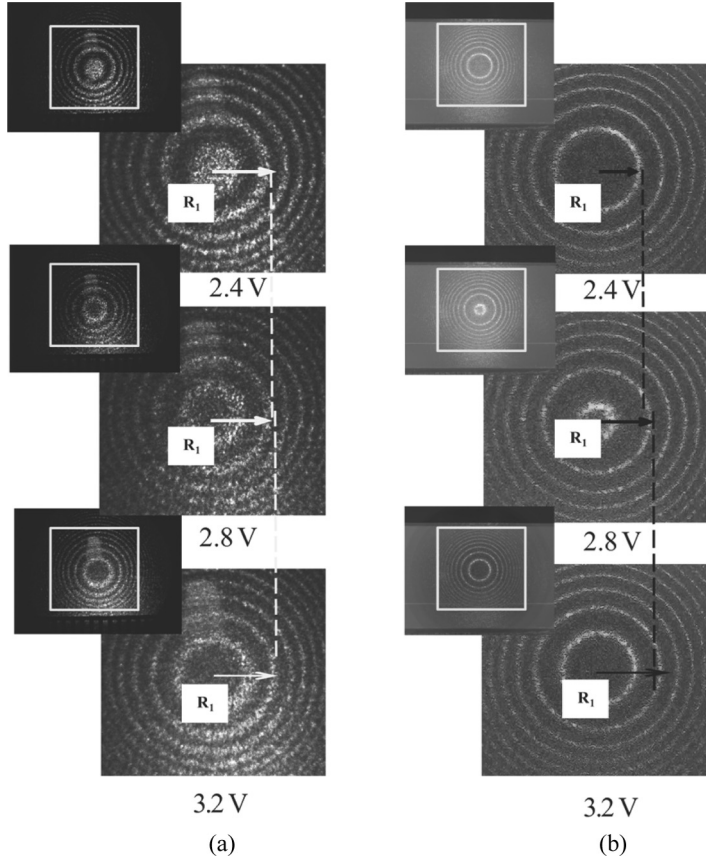


**Figure 2.** The dynamic fringe patterns measured by varying applied voltages where the image plane was flat and parallel to the LC-FP cell as shown in Figure 1(a). The images of (a) and (b) are obtained by using the LC-FP cells with the same cell conditions used in obtaining the left and right images of Figure 1(b), respectively.

the same variation of an applied voltage were larger in the cell with  $d_{lc} = 15 \mu\text{m}$  because we can obtain larger variation of the effective refractive index of the LC layer at the same voltage condition as the thickness of the LC layer becomes larger. The fact that the field-induced tilting angle of the LC layer can be sufficiently small in the whole driving voltages for scanning is another merit suitable for getting circularly symmetric ring patterns irrespective of applied voltages. Hereafter, the experimental results were ones obtained with the NLC-FP cell made by the thicker cavity ( $d_{lc} = 15 \mu\text{m}$ ) and the higher reflective mirror (95%).

### Measurement Principle and Experimental Results

In our surface scanning method, the real surface map is obtained by analyzing the distortions from the ideal ring fringe patterns which can be obtained in a flat surface as shown in Figure 2. The derived ideal ring fringe patterns are used as the reference fringe patterns in analyzing the surface profile and we should know the reference fringe patterns from the resonant mode analysis.

In our NLC-FP cell, the resonant mode equation at the center can be expressed as

$$2d_{lc}n_{eff}(v) + 2d_gn_g \pm \frac{\lambda}{2} = (m_1 + e)\lambda + 2d_{lc}\Delta n_{eff} \quad (3)$$

where  $m_1$ ,  $e$  ( $0 < e < 1$ ), and  $\lambda$  are the resonant mode number of the innermost bright fringe ring, the fractional order at the center, and the wavelength of the incident light ( $\lambda = 632.8$  nm) [13].

For the  $p$ th bright fringe ring by the slightly diverging rays, the resonant mode condition of Eq. (3) can be modified as follows,

$$\begin{aligned} 2d_{lc}(n_{eff}(v) \cos \phi_{lc}) + 2d_gn_g \cos \phi_g \pm \frac{\lambda}{2} \\ = m_p\lambda = [m_1 - (p - 1)]\lambda, \quad (p: 1, 2, 3, \dots) \end{aligned} \quad (4)$$

where  $m_p$  is the resonant mode order of the  $p$ th bright fringe ring. Hence, we can express the resonant condition of the  $p$ th bright fringe ring in a form that the resonant mode number is removed from Eqs. (3) and (4) as follows,

$$2d_{lc}n_{eff}(v) \frac{\phi_{lc}^2}{2} + 2d_gn_g \frac{\phi_g^2}{2} = (p - 1 + e)\lambda + 2d_{lc}\Delta n_{eff} \quad (5)$$

By using the Snell's law and the lens equation,  $\phi_p$  and  $D_p$  of the  $p$ th bright fringe ring is obtained as follows,

$$\phi_p^2 = \frac{n_{eff}(v)n_g[(p - 1 + e)\lambda + (2d_{lc}\Delta n_{eff})]}{(n_gd_{lc} + n_{eff}(v)d_g)} \quad (6)$$

$$D_p^2 = (2f\phi_p)^2 = 4f^2 \frac{n_{eff}(v)n_g[(p - 1 + e)\lambda + (2d_{lc}\Delta n_{eff})]}{(n_gd_{lc} + n_{eff}(v)d_g)} \quad (7)$$

where  $\phi_p$  is the angle between the normal incident ray and the ray constructing the  $p$ th bright fringe ring as shown in Figure 3.  $D_p$  is the diameter of the  $p$ th bright fringe ring.  $f$  is the focal length of the lens. As a result, the real surface profile can be obtained as follows,

$$h = \Delta R_p \times \cot\left(\frac{R_{p,reference}}{f}\right) \quad (8)$$

$$\Delta R_p = (R_{p,reference} - R_{p,measure}) \quad (9)$$

where  $R_{p,reference}$  and  $R_{p,measure}$  are the radius of the  $p$ th bright fringe ring of the reference fringe patterns and the measured fringe patterns, respectively.  $h$  is the calculated surface depth measured at the  $p$ th bright fringe ring from the difference of  $R_{p,reference}$  and  $R_{p,measure}$ .

Figure 4 shows  $R_p$  as a function of the effective refractive index of the NLC layer where the filled circle and the line denote the measured results and the simulation

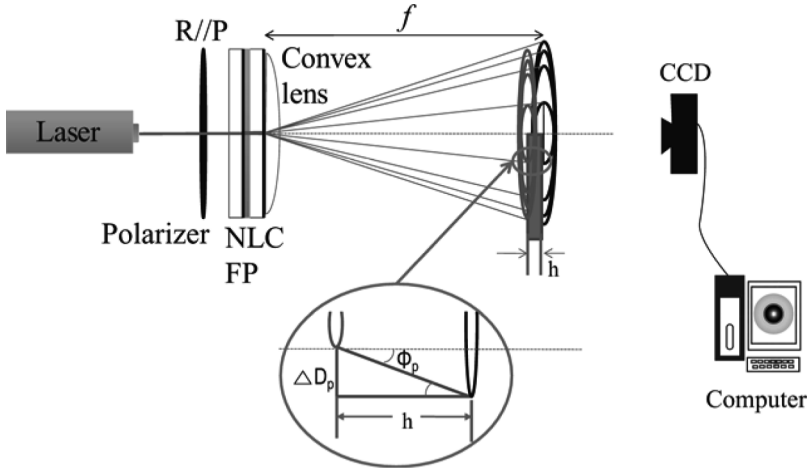


**Figure 3.** Schematic diagram showing the real surface profile measurement from the projected dynamic fringe patterns using our NLC-FP cell.

results from Eq. (7), respectively. In our measurement of  $R_p$ 's from the projected images, the average values from the radius values with the half-maximum intensity at each fringe peak were used. In the experimental results of Figures 4 and 5, the bar and the dot symbols represent the radius values with the half-maximum intensity at each peak and  $R_p$ 's from the average value, respectively.

Because the effective refractive index increases as an applied voltage increases,  $D_p$  also continuously increases as derived in Eq. (7) until a new innermost bright

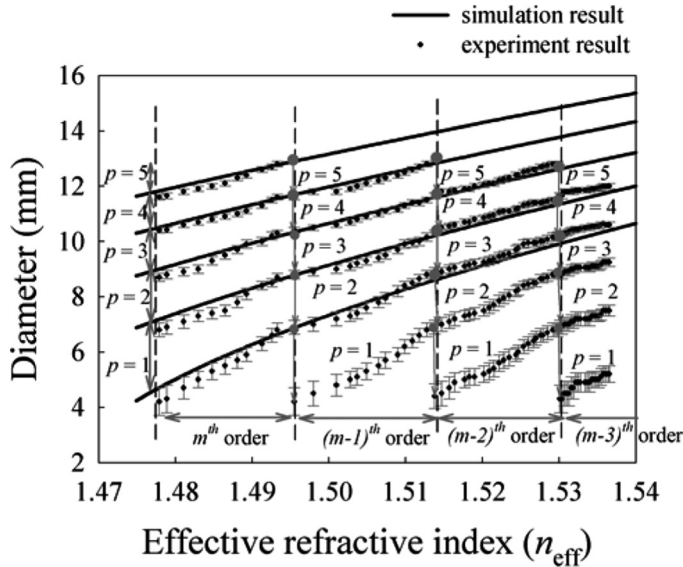


**Figure 4.** Plot of  $R_p$  as a function of the effective refractive index of the NLC layer where the dot and the line denote the measured results and the simulation results from Eq. (7), respectively.



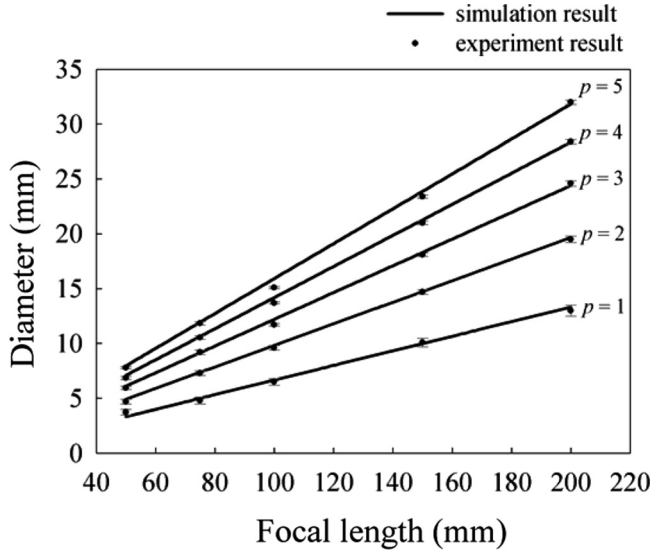


**Figure 5.** Plot of diameter of the  $p$ th fringe patterns versus the focal length of the convex lens used for projection of the fringe patterns where the filled circle and the line denote the measured results and the simulation results from Eq. (7), respectively.

fringe ring is generated. Figure 4 shows small amount of the effective refractive index variation is required to scan the whole area with moving fringes. In our sample, the required effective refractive index was about 0.02, which can be obtained with small bias tilting angles of LC molecules. The simulated results using Eq. (7) match well with the measured results, which show we can construct multiple sets of the reference fringe patterns theoretically with a high precision. In obtaining the experimental and simulation results of Figure 4, the focal length of the used convex lens was 75 mm. The fractional order at the center,  $e$  was 0.625 in calculation.

Figure 5 shows  $D_p$  variation as a function of focal lengths of lens used for projection of the fringe patterns where the filled circles and the lines denote the measured results and the simulation results from Eq. (7), respectively. The focal length of a convex lens can control the projection area for measuring. At a given line width of fringe patterns, the sampling number through the scanning is also determined by the focal length of the convex length.

We can reconstruct a real surface profile from sets of the fringe pattern distortions by using Eqs. (8) and (9) as shown in Figure 6. Figure 6(a) shows the object surface profile used in our experiment. Figures 6(b) and (c) show the distorted fringe patterns projected on the object shown in Figure 6(a) at applied voltage conditions of 0 V and 2.8 V, respectively. Figure 6(b) shows that the radius of the first bright ring pattern is distorted in the projected region with the depth difference by 1 mm. The second bright ring is distorted also in the projected region with the same depth difference. When we consider the reference plane as the lowest surface shown in Figure 6(a), the fringe patterns in the left part of Figure 6(b), with undistorted ring shape, can be the reference fringe patterns at analyzing depth profile in each  $p$ th order projection pattern. When we extracted the depth information along the distorted first ring pattern, the first depth,  $h$  of the object was 0.9998 mm from

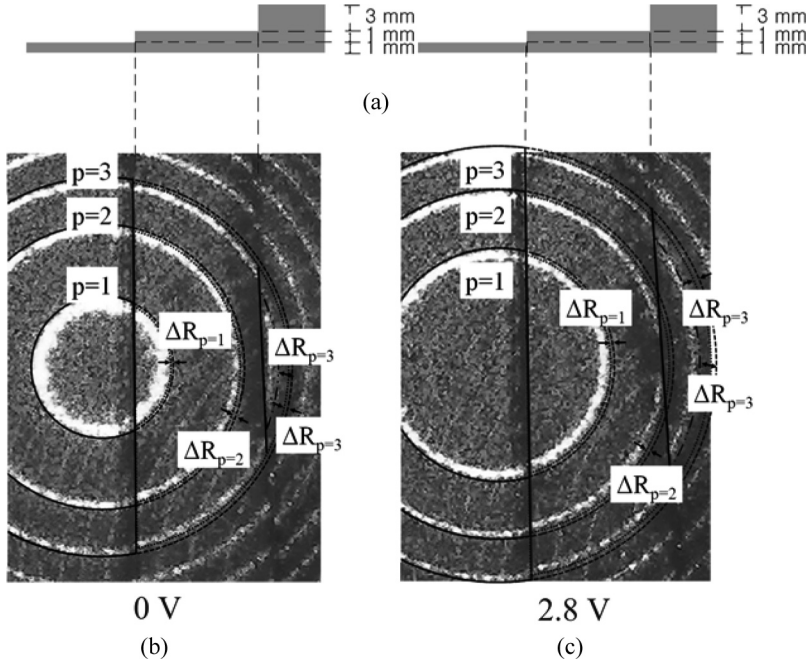


**Figure 6.** (a) The real surface profile of the object used in our experiment. (b) and (c) are the distorted fringe patterns projected on the object at applied voltage conditions of 0 V and 2.8 V, respectively.

Eqs. (8) and (9) by using the radius of the reference ring,  $R_1 = 2.2$  mm and the distortion amount of the radius,  $\Delta R_1 = 0.02$  mm. When the same depth was obtained along the line of the second ring pattern, the measured values were  $R_2 = 4.15$  mm and  $\Delta R_2 = 0.05$  mm. Thus, the extracted depth was 1.2 mm. In case of  $p = 3$ , the distortions of  $R_3$  was appeared twice with the depth differences from the reference plane by 1 mm and 4 mm. When we measured the 1 mm depth along the third fringe ring, the extracted depth was 1.0998 from the values of  $R_3 = 6.26$  mm and  $\Delta R_3 = 0.06$  mm. We could get the depth of 4 mm also with the distortion of the third ring pattern where the calculated depth was 4.03 mm from  $\Delta R_3 = 0.22$  mm. The extracted depth values matched well with the real surface profile. To obtain the observing whole area, sets of distorted patterns can be used as shown in Figure 6(c).

## Conclusions

We demonstrated the optical surface scanning profilometer by using an electrically tunable LC-FP cell. The LC-FP cell can generate multiple sets of circularly symmetric fringe ring patterns as reference patterns within relatively low driving voltages by using the electrically controllable effective refractive index of the LC layer in extraordinary rays. The resonant mode analysis shows that the real surface profile can be obtained by analyzing the amount of distortions of the projected fringe patterns. We expect our 3-D optical surface profilometer device and our scanning method would be a useful tool for miniaturized medical imaging applications such as 3D tooth-form scanning systems [4,5].

## Acknowledgments

This research was financially supported by the Korea Science and Engineering Foundation (KOSEF) grant funded by the Korea government (2009-0088705) and Basic Science Research Program through the National Research Foundation of Korea (NRF) grant funded by the Korea government (MEST) (2010-0001884).

## References

- [1] Su, X., & Chen, W. (2001). *Opt. Lasers Eng.*, 35, 263.
- [2] Mauvoisin, G., Bremand, F., & Lagarde, A. (1994). *Appl. Opt.*, 33, 2163.
- [3] Meng, X. F., *et al.* (2006). *Opt. Lett.*, 31, 1046.
- [4] Chen, L. C., & Huang, C. C. (2005). *Meas. Sci. Technol.*, 16, 1061.
- [5] Buytaert, J. A. N., & Dirckx, J. J. J. (2008). *Opt. Express*, 16, 179.
- [6] Patel, J. S., *et al.* (1990). *Appl. Phys. Lett.*, 57, 1718.
- [7] Patel, J. S., & Lee, S.-D. (1991). *Appl. Phys. Lett.*, 58, 2491.
- [8] Patel, J. S., & Maeda, M. W. (1991). *IEEE Photonics Technol. Lett.*, 3, 739.
- [9] Patel, J. S. (1991). *Appl. Phys. Lett.*, 59, 1314.
- [10] Lee, J.-H., Kim, H.-R., & Lee, S.-D. (1999). *Appl. Phys. Lett.*, 75, 859.
- [11] Lee, J.-H., Kim, H.-R., & Lee, S.-D. (1999). *Mol. Cryst. Liq. Cryst.*, 337, 19.
- [12] Kim, H.-R., Lee, J.-H., & Lee, S.-D. (2001). *Mol. Cryst. Liq. Cryst.*, 368, 45.
- [13] Born, M., *et al.* (1975). *Principles of Optics*, Oxford: Pergamon, UK.
- [14] Mcadams, L. R., Mcruer, R. N., & Goodman, J. W. (1991). *Opt. Lett.*, 16, 864.